Modelling of Over-Tip-Rotor liners for the suppression of rotor-alone fan noise

Sergi Palleja-Cabre*, Brian J. Tester†, and R. Jeremy Astley‡
Institute of Sound and Vibration Research, University of Southampton, Southampton, SO17 1BJ, UK

Fan noise is one of the dominant sources of aircraft engine noise, both at approach and at take-off. Improved attenuation of fan noise with acoustic liners and the reduction of fan noise at source remain key technology challenges for civil aviation in the foreseeable future. Over-Tip-Rotor (OTR) acoustic treatments have been investigated experimentally during the last decade and significant fan noise reductions have been measured, most recently using a single rotor and multiple lined circumferential grooves. This paper describes an analytical OTR prediction model in which the fan noise is modelled with point or distributed, static or rotating monopole and dipole sources based on Green's functions for infinite hard or lined cylindrical ducts containing uniform mean flow; these are combined with an anechoic or unflanged inlet termination and an embedded finite length lined section in which the 'rotor-alone' source is located with its OTR liner. OTR liner insertion loss predictions are obtained for comparison with data from the W-8 NASA experimental rig. These yield peak broadband in-duct noise reductions of up to 4 dB, in line with the measurements.

Nomenclature

a	=	duct radius
f	=	frequency / external force
m, n	=	azimuthal and radial modal orders
p	=	acoustic pressure
u	=	acoustic particle velocity
x, r, θ	=	axial, radial and circumferential coordinate
G	=	Green's function of pressure
J_m,Y_m	=	Bessel functions of the first and second kind
M	=	Mach number

*Research Fellow, Acoustics Group, Institute of Sound and Vibration Research.
†Principal Research Fellow, Acoustics Group, Institute of Sound and Vibration Research. Senior Member AIAA.
‡Emeritus Professor, Acoustics Group, Institute of Sound and Vibration Research. Senior Member AIAA.
Presented as Paper 2021-2242 at the AIAA AVIATION 2021 FORUM, Virtual Event, August 2–6

R	=	specific acoustic resistance
S_{ff}, S_{pp}	=	source / pressure cross-spectrum
U_c	=	convection velocity
Z	=	specific acoustic impedance
α, κ	=	radial and axial wave number
γ	=	dipole alignment w.r.t the duct axis
ϕ_{ff}	=	wall pressure spectrum
ω	=	angular frequency
Θ	=	stagger angle
$\bar{\Omega}$	=	fan rotor angular frequency

I. Introduction

The turbofan engine, used in most medium to long range aircraft, is a significant contributor to the overall aircraft noise. In modern high-bypass-ratio designs, fan noise is one of the dominant engine sources both at approach and at take-off and a critical noise-reduction target for the next generation of turbofan engines.

Passive acoustic treatments or duct liners are a well-known and efficient way to attenuate fan noise. Maximising the treated area is a key parameter in improving liner performance. Over-Tip-Rotor (OTR) acoustic treatments have been investigated during the last decade as a technology with the potential to increase liner area. Significant noise reductions have been measured [1–3]. The noise reduction mechanisms of OTR liners are attributed to a combination of (1) conventional absorption of acoustic waves propagating over the liner, (2) modification of the source itself caused by the liner boundary condition in the vicinity of the rotor-blade tip [1] and, (3) reduction in the fan/OGV (Outlet Guide Vane) interaction noise possibly due to a reduction of the turbulence intensity in the fan wake caused by the OTR liners [4].

The use of circumferential grooves as part of the OTR acoustic treatment has been adopted at NASA as a potential method for reducing losses in fan aerodynamic performance while protecting the structural integrity of the rotor blades and the liner. Acoustically treated grooves tested in the W-8 Single-Stage Axial Compressor Facility at the NASA Glenn Research Center showed that the loss in adiabatic efficiency of the fan was within the measurements repeatability margin [4], in contrast to earlier OTR liner designs where it was reported to be as high as 9.3% [5].

Previously published research has concentrated on experimental studies of OTR liners. Analytical models to predict their acoustic performance and to estimate the optimum liner impedance are not currently available. A related problem of modelling the interaction between a liner installed in the bypass region close to an OGV has been recently studied in [6]. A transfer element method (TEM) and a three-dimensional lifting-surface method were used to capture the sound generation and propagation simultaneously. Although that work does not involve OTR liners, it shows that the coupling

of the liner and nearby sound sources should be considered when targeting the liner optimum impedance. A recent study on the reduction of tip noise sources with an over-tip liner has been reported in [7] using a static aerofoil. It shows that the noise reduction benefits of over-tip liners are greater when the noise sources are close to the liner surface.

This paper focuses on a comparison of results obtained with an analytical prediction model for the noise reduction performance of OTR liners and measured data acquired in the NASA W-8 test rig [8]. The model presented here includes the coupling of the fan sources to sound propagation and noise suppression. Green's functions are used for this purpose, building upon previous analytical studies [9, 10]. Improvements to previous work include modelling of an inlet termination and of distributed rotating sources.

The rest of the paper is organised as follows. The analytical model for the noise sources, duct propagation and attenuation is described in Section II, with emphasis on the new additions relative to the model in [10], and analytical modelling of the circumferential grooves used in the W-8 NASA tests in Section III. A comparison between the predicted and measured Insertion Loss for the OTR liners is shown in Section IV. Finally, the suitability of an anechoic or unflanged inlet termination to model the W-8 test rig bellmouth analytically is explored in Section V by comparing the predictions with reference FE solutions. A comparison of the impedance prediction model with the measured data can be found in Appendix A. Key aspects of the experimental data and its implications for the comparison with the analytical model are presented in Appendix B.

II. Modelling of the noise sources, duct propagation and attenuation

In this section an analytical Green's function model termed 'Green/FINF' is described for a Finite length liner connected to INFinite hard wall extensions. A diagram of the problem is shown in Fig. 1. This model provides a simplification for a rotor-alone configuration with (1) the OTR liner modelled by a finite lined section, and (2) the fan noise source modelled with point or distributed, static or rotating monopole and dipole sources *within* the lined section. The model is based on Green's functions for lined cylindrical ducts. An inlet termination is modelled by modal reflection coefficients at the upstream boundary. The main assumptions of the model are summarised in Table 1.

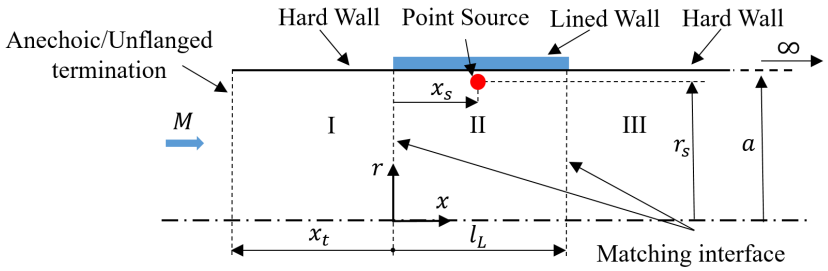

Fig. 1 Diagram of the simplified Over-Tip-Rotor problem considered for the Green/FINF model.

Locally reacting in the axial direction and non-locally reacting in the azimuthal direction, as described in [11].

Table 1 Main assumptions of the analytical OTR liner prediction model.

Geometry	Axially segmented hollow circular duct with anechoic/unflanged inlet and anechoic outlet
Propagation	Linear
Mean flow	Uniform or 'plug' flow
Impedance	Ingard-Myers boundary condition and locally or 'semi-locally' reacting liners
Source	Point/distributed static/rotating monopoles/dipoles

A. Acoustic field generated by ducted static sources

The acoustic field generated at $\mathbf{x} = (x, r, \theta)$ by a distribution of dipoles $\boldsymbol{f}(\mathbf{y})$ located at $\mathbf{y} = (x_s, r_s, \theta_s)$ on a 'blade' surface S within the lined section of a duct is given by the non-dimensional version of the Goldstein acoustic analogy in the frequency domain [12]

$$p(\mathbf{x}, \omega) = \iint_S f(\mathbf{y}, \omega)\hat{\mathbf{n}} \cdot \nabla_y G(\mathbf{x}|\mathbf{y}) dS(\mathbf{y}) \quad , \tag{1}$$

where f is the strength of the dipole assumed to lie normal to the blade surface S, and G is a customised Green's function which satisfies the duct boundary conditions. The $e^{j\omega t}$-convention is used throughout this paper. The normal $\hat{\mathbf{n}}$ for a flat plate assumption is given by

$$\hat{\mathbf{n}} = [\hat{x}, \hat{r}, \hat{\theta}] = [\cos\gamma, 0, \sin\gamma] \quad , \tag{2}$$

where $\gamma(r_s)$ is the angle of the blade normal to the duct axis, which is assumed to be slowly varying along the radius. The Green's function G is given Rienstra & Tester [13] for a lined circular duct with uniform mean flow as a sum of non-orthogonal modes

$$G(\mathbf{x}|\mathbf{y}) = \sum_{m=-\infty}^{\infty} e^{-jm(\theta-\theta_s)} G_m(r, x) \quad , \tag{3}$$

where

$$G_m(r, x) = \sum_{n=1}^{\infty} G_{mn} = \sum_{n=1}^{\infty} -\frac{1}{2\pi j} \frac{J_m(\alpha^{\pm}_{mn} r) J_m(\alpha^{\pm}_{mn} r_s)}{Q^{\pm}_{mn} J_m(\alpha^{\pm}_{mn})^2} e^{-j\kappa^{\pm}_{mn}(x-x_s)} \quad , \tag{4}$$

with

$$Q^{\pm}_{mn} = \pm \left[(\kappa^{\pm}_{mn} + \Omega^{\pm}_{mn} M) \left(1 - \frac{m^2}{\alpha^{\pm 2}_{mn}} - \frac{\Omega^{\pm 4}_{mn}}{(\omega \alpha^{\pm}_{mn} Z)^2} \right) - \frac{2jM\Omega^{\pm}_{mn}}{\omega Z} \right] \quad , \tag{5}$$

which yields

$$p(\mathbf{x}, \omega) = \iint_S f(\mathbf{y}, \omega) \sum_{m=-\infty}^{\infty} e^{-jm(\theta-\theta_s)} \left(j \sum_{n=1}^{\infty} G_{mn} \left[\kappa^{\pm}_{mn} \cos\gamma + \frac{m}{r_s} \sin\gamma \right] \right) \quad . \tag{6}$$

$Q^{\pm}_{mn}$, $\alpha^{\pm}_{mn}$ and $\kappa^{\pm}_{mn}$ are used for the right-running (+) and left-running modes (-), in the regions $x > x_s$ and $x < x_s$ respectively and $\Omega^{\pm} = \omega - \kappa^{\pm} M$. The radial and axial modal wavenumbers, $\alpha^{\pm}_{mn}$ and $\kappa^{\pm}_{mn}$, are obtained by finding the solutions of the eigenvalue equation as detailed in [13]. It is noted that Eq. 6 is singular at the cut-on/cut-off frequency

of each mode, which is considered in more detail in section V. This formulation is used for predicting the sound field for any locally reacting specific acoustic impedance (Z) but is also applied here to the case of a semi-locally reacting liner impedance such as the acoustically treated grooves described in [11] and addressed in this paper for the comparison with the W-8 data.

Similarly, it can be shown that the pressure field excited by a distribution of static volume velocity monopole sources over the surface S is given by

$$p(\mathbf{x},\omega) = \iint_S Q(\boldsymbol{y},\omega) \sum_{m=-\infty}^{\infty} e^{-jm(\theta-\theta_s)} \left(- j \sum_{n=1}^{\infty} \Omega_{mn} G_{mn} \right) \quad , \tag{7}$$

where Q is the volume velocity source strength. This expression has been used in this paper solely for comparison with the FE solution in Section V since monopole sources are more easily implemented in the software Simcenter 3D [14].

B. Acoustic field generated by ducted rotating sources

The effect of the dipole rotation is included in the Green's function approach by expressing the azimuthal source position $\theta_s(\tau)$ in the stationary frame of reference relative to the duct as

$$\theta_s(\tau) = \tilde{\theta}_s + \bar{\Omega}\tau \quad , \tag{8}$$

where $\tilde{\theta}_s$ is the source azimuthal position in a rotating frame of reference spinning with the fan at a non-dimensional angular frequency $\bar{\Omega}$ and τ denotes emission time. All variables with tilde notations are expressed in the rotating frame.

The time domain version of Eq. 1 [12] is expressed as

$$p(\boldsymbol{x},t) = \int_{-\infty}^{\infty} \iint_S f(\boldsymbol{y},\tau) \hat{\mathbf{n}} \cdot \nabla_y g(\boldsymbol{x},t|\boldsymbol{y},\tau) dS(\boldsymbol{y}) d\tau \quad , \tag{9}$$

where $g(\boldsymbol{x},t|\boldsymbol{y},\tau)$ is the Green's function in the time domain. The relationship between the time and frequency domain Green's functions g and G is given by the inverse Fourier transform [12]

$$g(\boldsymbol{x},t|\boldsymbol{y},\tau) = \frac{1}{2\pi} \int_{-\infty}^{\infty} G(\boldsymbol{x}|\boldsymbol{y}) e^{j\omega(t-\tau)} d\omega \quad . \tag{10}$$

Substitution of Eq. 8, Eq. 10 and the frequency domain Green's function (Eq. 3) into Eq. 9 yields

$$p(\boldsymbol{x},t) = \int_{-\infty}^{\infty} \iint_S f(\tilde{\boldsymbol{y}},\tau) \frac{1}{2\pi} \int_{-\infty}^{\infty} \hat{\mathbf{n}} \cdot \nabla_y \left[\sum_{m=-\infty}^{\infty} e^{-jm(\theta-\theta_s(\tau))} G_m(\boldsymbol{x}|\tilde{\boldsymbol{y}}) e^{j\omega(t-\tau)} \right] d\omega dS(\tilde{\boldsymbol{y}}) d\tau \quad , \tag{11}$$

which can be re-written as;

$$p(\boldsymbol{x},t) = \int_{-\infty}^{\infty} \iint_{S} f(\tilde{\boldsymbol{y}},\tau) \frac{1}{2\pi} \int_{-\infty}^{\infty} \hat{\mathbf{n}} \cdot \nabla_y \left[\sum_{m=-\infty}^{\infty} e^{-jm(\theta-\tilde{\theta}_s)} G_m(\boldsymbol{x}|\tilde{\boldsymbol{y}}) e^{j\omega t} e^{-j(\omega - m\bar{\Omega})\tau} \right] d\omega dS(\tilde{\boldsymbol{y}}) d\tau \quad , \tag{12}$$

where G_m is given by Eq. 4. The integral over the emission time gives

$$\int_{-\infty}^{\infty} f(\tilde{\boldsymbol{y}},\tau) e^{-j(\omega - m\bar{\Omega})\tau} d\tau = f(\boldsymbol{y}, \omega - m\bar{\Omega}) \quad , \tag{13}$$

which yields

$$p(\boldsymbol{x},t) = \iint_{S} \frac{1}{2\pi} \int_{-\infty}^{\infty} \sum_{m=-\infty}^{\infty} f(\tilde{\boldsymbol{y}}, \omega - m\bar{\Omega}) \hat{\mathbf{n}} \cdot \nabla_y \left[e^{-jm(\theta-\tilde{\theta}_s)} G_m(r,x) \right] e^{j\omega t} d\omega dS(\tilde{\boldsymbol{y}}) \quad . \tag{14}$$

The pressure field at the observer position due to a distribution of rotating dipoles in the frequency domain can then be obtained by taking the Fourier transform and applying the gradient:

$$p(\mathbf{x},\omega) = \iint_{S} \sum_{m=-\infty}^{\infty} e^{-jm(\theta-\tilde{\theta}_s)} \left(j f(\tilde{\boldsymbol{y}}, \omega - m\bar{\Omega}) \sum_{n=1}^{\infty} G_{mn} \left[\kappa_{mn}^{\pm} \cos\gamma + \frac{m}{r_s} \sin\gamma \right] \right) dS(\tilde{\boldsymbol{y}}) \quad . \tag{15}$$

Comparison of the equation above with its counterpart for a static dipole (Eq. 6) shows that the effect of the source rotation is to shift the frequency ω of the source strength term by $-m\bar{\Omega}$ but does not modify the propagation terms in the Green's function, which are still evaluated at ω. The physical interpretation of this result is that the unsteady perturbations will generate broadband noise that will be perceived to have a frequency ω in the static frame of reference but which are generated with a shift of $-m\bar{\Omega}$ in the rotating frame of reference. Therefore, the source strength and its propagation become coupled through the azimuthal mode number. The current modelling of the source rotation does not account for the swirling flow induced by the fan rotation. Equivalent expressions for the hard wall Green's function have been derived in the literature by, amongst others, Ventres [15] and Lowis et al. [16]. Note that this solution requires the modelling or measurements of the dipole source strength spectrum, which is covered in more detail in Section II.D. Equivalent expressions following an analogous approach can be derived for rotating monopoles from Eq. 7 but have not been included here.

C. Inclusion of a termination in the mode-matching scheme

The total acoustic field at any point of the domain shown in Fig. 1 can then be obtained by imposing continuity of the unsteady mass and momentum at the two interfaces, I-II and II-III, and solving the resulting matching equations as detailed in [10]. The inclusion of reflections from a duct termination is implemented in the mode-matching model by assuming that the incident and reflected modes at the duct termination are linked by a reflection coefficient matrix

C. The complex amplitude of the reflected right-running modes can be obtained from the complex amplitudes of the left-running incident modes evaluated at the duct termination ($x = x_t$) as

$$A_{ml}^{I+} = \sum_{n=1}^{N} C_{mnl} A_{mn}^{I-} e^{-j\kappa_{mn}^{H-} x_t} \quad . \tag{16}$$

C_{mnl} relates the complex amplitude of the *incident* mode of azimuthal and radial order (m, n) with that of the *reflected* mode (m, l). Hence, the amplitude of the reflected mode (m, l), A_{ml}^{I+}, is the summation over all the contributions of the incident modes (m, n) allowing for radial scattering. The approach implemented here simply adds a set of equations to account for the new set of unknowns A_{mn}^{I+} previously set to zero in [10]. That is

$$\left[A_{mn}^{I+}\right] = \mathcal{R}\left[A_{mn}^{I-}\right] \quad , \tag{17}$$

where $\mathcal{R}$ is a full square matrix with elements

$$\mathcal{R}_{ij} = C_{mji} e^{-j\kappa_{mj}^{H-} x_t} \quad . \tag{18}$$

The reflection coefficients for an unflanged termination with flow have been obtained from the analytic Wiener-Hopf solution given by Munt [17, 18] and Rienstra [19]. This was evaluated using a code called GXMunt developed by Gabard and Astley [20], who extended the Munt solution to include an infinite centre body. The model has been applied to the inlet problem by setting the ambient and jet flow negative and equal and deactivating the Kutta condition at the edge controlling the vortex shedding since it is now assumed to be a leading edge. The introduction of a duct termination in terms of a matrix of reflection coefficients in the mode-matching scheme has been previously explored in the literature. Gabard and Astley [21] integrated their mode-matching formulation based on continuity of mass and momentum with the unflanged duct exhaust model outlined above, but with the focus on assessing the noise reduction in the far-field directivity rather than in the in-duct sound pressure level and power.

D. Modelling of the dipole strength function

The dipole strength function $f(\tilde{\boldsymbol{y}}, \omega)$ is required for a realistic estimate representative of a rotor blade. The modelling of fan self-noise is most suitably expressed, due to its broadband nature, in terms of the pressure cross-spectrum S_{pp} between two observer positions $\boldsymbol{x}$ and $\boldsymbol{x}'$ expressed as

$$S_{pp}(\boldsymbol{x}, \boldsymbol{x}', \omega) = \lim_{T \to \infty} \frac{\pi}{T} E\{p(\boldsymbol{x}, \omega) p^*(\boldsymbol{x}', \omega)\} \quad , \tag{19}$$

where * denotes the complex conjugate and $E\{\}$ the expectation value.

For a distribution of rotating dipole sources given by Eq. 15, the pressure cross-spectrum in a lined cylindrical duct with uniform mean flow can be expressed as

$$S_{pp}(\boldsymbol{x},\boldsymbol{x}',\omega) = \iint_{\tilde{S}}\iint_{\tilde{S}'}\sum_{m=-\infty}^{\infty}\sum_{m'=-\infty}^{\infty} S_{ff}(\tilde{\mathbf{y}},\tilde{\mathbf{y}}',\omega-m\bar{\Omega},\omega-m'\bar{\Omega})$$
$$G_m(\boldsymbol{x},\tilde{\mathbf{y}},\omega)G^*_{m'}(\boldsymbol{x}',\tilde{\mathbf{y}}',\omega)e^{-jm(\theta-\tilde{\theta}_s)}e^{jm'(\theta'-\tilde{\theta}'_s)}d\tilde{S}(\tilde{\mathbf{y}})d\tilde{S}'(\tilde{\mathbf{y}}') \quad , \quad (20)$$

where

$$S_{ff}(\mathbf{y},\mathbf{y}',\omega,\omega') = \lim_{T\to\infty}\frac{\pi}{T}E\{f(\mathbf{y},\omega)f^*(\mathbf{y}',\omega')\} \quad , \quad (21)$$

is the source spatial and frequency cross-spectrum, which is often based on models of the boundary layer pressure fluctuations on the blade surface [16, 22–24] due to Amiet's theory [25] of trailing edge noise in isolated blades.

The simplifying assumptions for the fan noise model that follows are based in the approach of Lowis et. al [16] and can be summarised as:

1) The acoustic sources of each blade are concentrated at the trailing edge ($x_s = x'_s$).
2) The fan consists of B identical uncorrelated blades.
3) Each rotor blade is considered a flat plate with zero pressure gradient.
4) The surface pressure fluctuations are assumed to be concentrated at the trailing edge and the scattering of the hydrodynamic pressure field as it sweeps past the trailing edge is not considered.
5) An additional assumption has been taken here to consider a homogeneous turbulent boundary layer such that

$$S_{ff}(\mathbf{y},\mathbf{y}',\omega,\omega') = S_{ff}(\mathbf{y},\mathbf{y}',\omega)\delta(\omega-\omega') \quad . \quad (22)$$

The source cross-spectrum can be rewritten from assumptions (1) and (2) as

$$S_{ff}(\mathbf{y},\mathbf{y}',\omega,\omega') = S_{ff}(r_s,r'_s,\theta_{s_0},\omega,\omega')\delta(\theta_{s_p}-\theta'_{s_p})\delta(\theta_{s_p}-2\pi p/B) \quad , \quad (23)$$

where θ_{s_p} is the azimuthal position of the trailing edge of each pth rotor blade.

The flat plate turbulence model used here to describe the spatial cross-spectrum follows assumptions (3)-(5) and is given by Blake [26] as

$$S_{ff}(r_s,r'_s,\omega) = \phi_{ff}(r_s,\omega)e^{-\bar{\gamma}\frac{\omega|r_s-r'_s|}{U_c}} \quad , \quad (24)$$

where ϕ_{ff} is the pressure spectrum of the turbulence boundary layer, $\bar{\gamma}$ is an experimental constant (typically 0.7 [16])

and U_c is the non-dimensional turbulent eddy convection velocity

$$U_c(r_s) = 0.7\sqrt{(\bar{\Omega} r_s)^2 + M_x^2} \quad . \tag{25}$$

where $\bar{\Omega}$ is the non-dimensional shaft angular frequency and M_x the Mach number of the axial uniform flow. The expressions implemented for ϕ_{ff} are the non-dimensional version of those in Appendix B of reference [16].

The final expression for the simplified pressure cross-spectrum for fan self-noise adopted in this paper can be obtained by substitution of Eq. 23-24 in Eq. 20 to yield

$$S_{pp}(\boldsymbol{x}, \boldsymbol{x}', \omega) = B \int_{r_s} \int_{r_s'} \sum_{m=-\infty}^{\infty} \phi_{ff}(r_s, \omega - m\bar{\Omega}) e^{-\tilde{\gamma}\frac{\omega|r_s - r_s'|}{U_c}} G_m(\boldsymbol{x}, \boldsymbol{y}, \omega) G_m^*(\boldsymbol{x}', \boldsymbol{y}') e^{-jm(\theta - \theta_s)} r_s r_s' dr_s dr_s' \quad . \tag{26}$$

The integrals over the source region S and S' in the pressure cross-spectrum of Eq. 20 are reduced to integrals over the radial source position due to assumptions (1) and (2) expressed in Eq. 23. Assumption (5) reduces the double summation over m and m' to a single sum over m. The two integrals are discretised and evaluated numerically. Note that the variables involved in ϕ_{ff} vary for each radial source position, which means that the radial distribution of source strength is affected by $\bar{\Omega}$, the spanwise rotor-blade chord distribution and frequency. The simplifying assumptions considered in the modelling of the fan noise sources are aimed at capturing the general characteristics of the source for the prediction of OTR liner noise reductions. It is however not a comprehensive representation of the broadband fan noise sources that can lead to discrepancies with the measured data but represents the starting point for future more complex studies.

III. Modelling of the liner configurations

The acoustically treated circumferential grooves tested in the NASA W-8 rig [3] cover the axial projection of the fan chord, as shown in Fig. 2a. The grooves are formed of upper and lower parts as indicated in the diagram in Fig. 2b. The upper part ② is open at the top and terminated at the base with a hard or porous 'septum'. Below the septum, the lower part of the groove ① is partitioned azimuthally. The equivalent groove impedance at the main duct - groove interface Z_g can be obtained by using the analytical groove model described in [9, 11]. It is given by

$$Z_g(\omega, m) = -j\frac{J_m(\omega) + K_m Y_m(\omega)}{J_m'(\omega) + K_m Y_m'(\omega)} \quad , \tag{27}$$

where

$$K_m = -\frac{J_m'(\omega[1+d]) + j\frac{J_m(\omega[1+d])}{Z_f}}{Y_m'(\omega[1+d]) + j\frac{Y_m(\omega[1+d])}{Z_f}} \quad . \tag{28}$$

Z_f is the locally reacting impedance at the septum, and d is the groove depth. Note that Z_g depends on the azimuthal order m of the pressure component to which it is applied. In this sense it is termed 'semi-local' (a 'locally-reacting' liner would be independent of m).

Diagrams of the actual OTR liners tested in the W-8 rig are shown in Fig. 2c-2d. Note that a longitudinal cross-section parallel to the duct axis is used in Fig. 2b, i.e. the flow goes from left to right, whereas a transversal cross-section perpendicular to the duct axis is adopted in Fig. 2c-2d such that the flow direction is normal to the paper. A Single-Degree-Of-Freedom (SDOF) cavity liner is used with a 'thin' and 'thick' perforate in the configurations indicated in Fig. 2c-2d. It has been assumed that the impedance at the septum (Z_f) for the 'thin' and 'thick' perforates can be obtained by using the standard non-dimensional expression for a SDOF cavity liner [27]

$$Z_f = R_{fs} + j\left[\omega\frac{t+\varepsilon d_h}{\sigma} - \cot(\omega h)\right] \quad , \tag{29}$$

where R_{fs} denotes the resistance of the septum, t and d_h are the facing sheet thickness and hole diameter respectively, ϵ the end correction, σ the facing sheet porosity and h is the cavity depth. All variables are non-dimensional unless specified with a tilde.

The geometry of the grooves is specified in [3] and summarised in Table 2. The groove depth d is common for all configurations and the facing sheet and cavity parameters are also common for the 'thin' and 'thick' perforates, except for the facing sheet thickness, indicated as t_1 and t_2 respectively. The missing variable required in the analytical groove models is the facing sheet resistance R_{fs}, which is estimated by comparison to the measured impedance in the NASA Langley Normal Incidence Tube (NIT) [28]. Values of $R_{fs} = 0.5$ has been taken for the 'thin' perforate and $R_{fs} = 0.7$ for the 'thick' one. Details of this comparison are provided in Appendix A.

Table 2 Dimensional parameters of the acoustically treated grooves.

Liner #	$\tilde{l}_s$, in.	$\tilde{l}_g$, in.	$\tilde{d}$, in.	$\tilde{h}$, in.	$\tilde{t}$, in.	$\tilde{d}_h$	σ
1	1/8	1/4	1/2	1	0.06	0.035	0.1
2	1/8	1/4	1/2	1	1/4	0.035	0.1

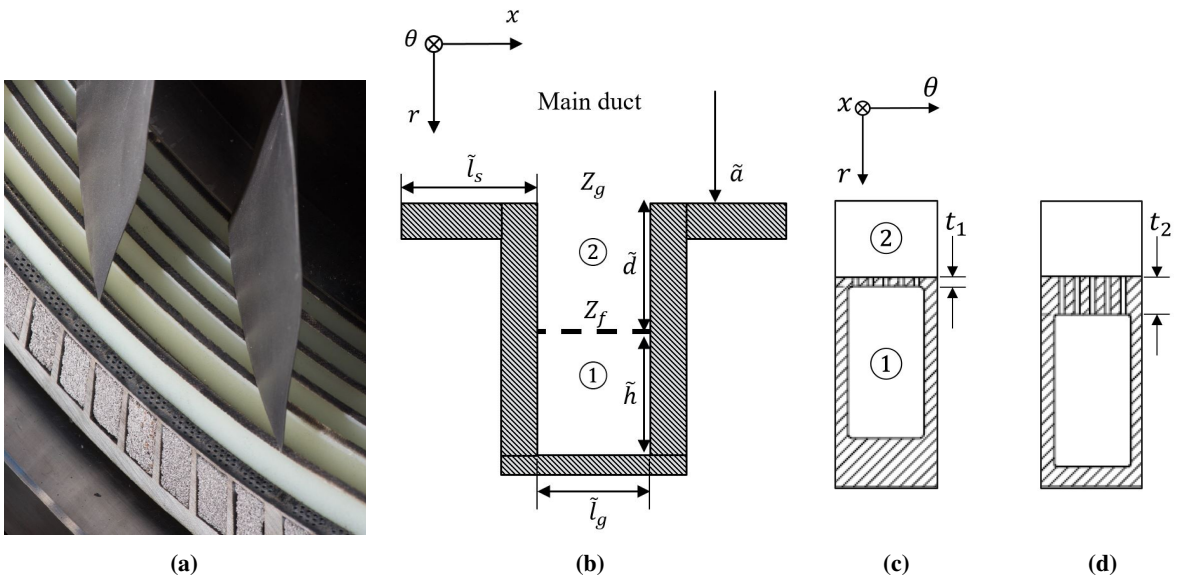

Fig. 2 OTR fan case liners: (a) View of the OTR fan case liner installed in the NASA W-8 fan rig [3], (b) dimensional diagram of the problem and nomenclature and actual geometry for configurations (c) 'Thin Perforate' and (d) 'Thick Perforate' [3].

IV. Comparison of predicted and measured Insertion Loss

The description of fan source model in section II is given for a fixed fan stagger angle ($\Theta=\pi/2-\gamma$) and without specifying a fan chord at each source radial location. The following assumptions are introduced for the analytical predictions in this section:

- **Stagger angle distribution $\Theta(r_s)$:** the fan chord at each radial location is assumed to be parallel to the incident flow such that

$$\Theta(r_s) = \text{atan}\left(\frac{\bar{\Omega} r_s}{M_x}\right) \quad . \tag{30}$$

- **Chord distribution $c(r_s)$:** the axial projection of the fan chord remains constant along the radius and equal to the OTR liner length l_L:

$$c(r_s) = \frac{l_L}{\cos[\Theta(r_s)]} \quad . \tag{31}$$

The measured axial mean flow at the fan section, $M_x = 0.236$, and the non-dimensional shaft rotation (or tip Mach number) at 50% fan speed, $\bar{\Omega} = 0.545$ have been used to determine the radial distribution of stagger angle and chord. In practice, for the OTR liner length in the W-8 test of $\tilde{l}_L$=57.2 mm, this results in Θ=30 deg. and $\tilde{c}$=66.0 mm at 25 % radius and Θ=66.6 deg. and $\tilde{c}$=143.9 mm at the fan tip.

The predicted SPL IL is obtained by averaging the pressure auto-spectrum $S_{pp}(\boldsymbol{x} = \boldsymbol{x'} = \boldsymbol{x}_{\text{mic}})$ for the hard (H) and lined (L) cases evaluated at the locations of the azimuthal microphone array in the W-8 rig $(x, r, \theta) = (-2.2a, a, \theta_{\text{mic}})$.

That is,

$$\text{SPL IL (dB)} = 10\log_{10}\left(\frac{\bar{S}_{pp,H}}{\bar{S}_{pp,L}}\right) \quad . \tag{32}$$

The non-dimensional acoustic axial power evaluated at the plane containing the microphone array is computed by numerically integrating the intensity field over the duct cross-section S [29]:

$$P(x) = \int_S I_x dS = \frac{1}{2}\int_S Re\left\{pu_x^*\left(1+M^2\right) + Mpp^* + Mu_x u_x^*\right\} dS \quad , \tag{33}$$

where the terms pp^*, pu^* and uu^* are estimated by the correspondent cross-spectral product S_{pp} given by Eq. 26 and the analogous expressions for S_{pu} and S_{uu}. The PWL IL is then obtained as

$$\text{PWL IL (dB)} = 10\log_{10}\left(\frac{P_\text{H}}{P_\text{L}}\right) \quad . \tag{34}$$

The main features of the OTR NASA W-8 test [3] and the measured data, used for the comparisons with the prediction model in this section, are discussed in Appendix B. Some key aspects of the measured data are however summarised below before showing the comparison of the predicted and measured noise reductions.

- Broadband background exhaust noise contaminates the data around 800 Hz and 4 kHz.
- Grooves generate additional broadband noise that becomes dominant at frequencies above 4 kHz.
- Leading edge (LE) broadband sources are likely to be significant in addition to trailing edge (TE) noise.

The groove noise is not modelled by the current analytical model, which assumes a uniform mean flow in the duct that does not interact with the grooves, nor the background exhaust noise. The comparisons between the measured and predicted noise reductions are therefore restricted to the frequency range of 1-3.5 kHz, for which groove noise is minimal and relatively free from the background exhaust noise (see Appendix B for details).

The broadband noise in this frequency range and rig operating conditions is within 100-120 dB (see Appendix B), which justifies the assumption of linear propagation intrinsic to the analytical model used in this paper. Non-linear effects occurring at higher fan speeds cannot be captured with the current model and are out of the scope of this study.

The measured pressure signals from the azimuthal microphone array are used to compare the measured and predicted noise reductions. The measured SPL IL are based on the SPL of the azimuthally averaged pressure at the wall for the hard wall baseline and lined configurations.

A. Anechoic inlet termination

The predictions in this section are made for an anechoic inlet termination. The main features of the measured data have been highlighted in the previous section. It has been argued that LE noise may well be a significant source contributor in the W-8 experiments. Therefore, noise predictions have been made for a source distribution located at

$x_s = 0.75l_L$, 'close' to the TE, and at $x_s = 0.25l_L$, 'close' to the LE. The chosen axial locations are sufficiently distant from the impedance discontinuity in the model to avoid convergence issues. Both source distributions are assumed to have the same strength and to be uncorrelated. A sensitivity study has shown marginal effects in the predicted noise reduction when placing the sources closer to the impedance discontinuity. In the absence of detailed information of the LE sources the same TE model described in Section II.D is used to estimate the contribution of the the LE sources.

The predictions for the 'thin' and 'thick' perforates are compared to the W-8 measured data in Fig. 3. Leaving aside the multiple spikes in the predicted spectra, which will be discussed shortly, and focusing on the trend line for broadband, noise reductions of up to 6 dB are predicted in Fig. 3a when the source plane is located closer to the TE. A longer lined surface is then available between the source and the upstream measurement plane than for the case when LE and TE sources are present. The measured IL is however overpredicted by up to 4 dB over the range 1.5-2.5 kHz. When the sources are divided between the LE and the TE, the predicted IL is reduced and more closely approximates the measured data, the LE sources being less attenuated by the OTR liner. Analogous trends can be observed in Fig. 3b for the 'thick' perforate configuration, although the predicted and measured IL are in closer agreement.

The sharp spikes in the SPL IL spectra which are an important feature of the predicted data are due to modes cutting on. These are not evident in the measured data. Weaker, broader peaks and troughs are however present in the measured spectrum with similar frequency spacing to the sharper analytic spikes. This led the authors to speculate whether this is associated with differences in the duct termination conditions or duct geometries (or both) in the Green/FINF model and the W-8 data. The effect of an anechoic versus an unflanged inlet termination is discussed in greater detail in part B of this section, and the effect of the bellmouth geometry of the W-8 rig is discussed in section V to follow. At this point of the analysis, by ignoring the spikes and keeping in mind the ±1 dB repeatability of the experiments, a reasonable agreement in magnitude and spectral shape can be drawn from the comparisons of the predicted and measured data consistent across the two liner configurations.

Based on the results shown here for the 'thin' perforate for a TE source or a LE and TE source, it is surmised that the chordwise location of the source mechanism is the key parameter in determining the peak noise reductions, the OTR liner being more effective for TE noise. Additional predictions not shown here indicate that the radial distribution of source strength also has an important effect, the maximum noise benefit coming from radial distributions where the source is concentrated close to the OTR liner.

With regard to the sharp frequency spikes in the predicted SPL results of Fig. 3, the PWL is known to be less affected than SPL by singularities at the cut-on frequencies of the duct modes. Joseph et. al. [30] defined expressions that relate the axial acoustic power in a hard wall duct with the averaged pressure across the duct cross-section for various distributions of uncorrelated sources. That work also proposed a relationship between the averaged pressure across the duct and that observed at the wall. There is also evidence from [30] that the SPL IL at the wall is a good

Suggested by Professor Morfey (Personal Communication).

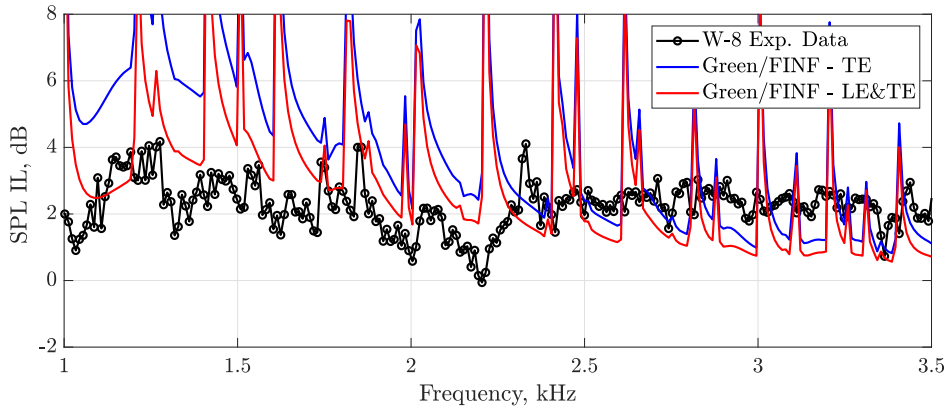

(a) 'Thin' perforate OTR configuration

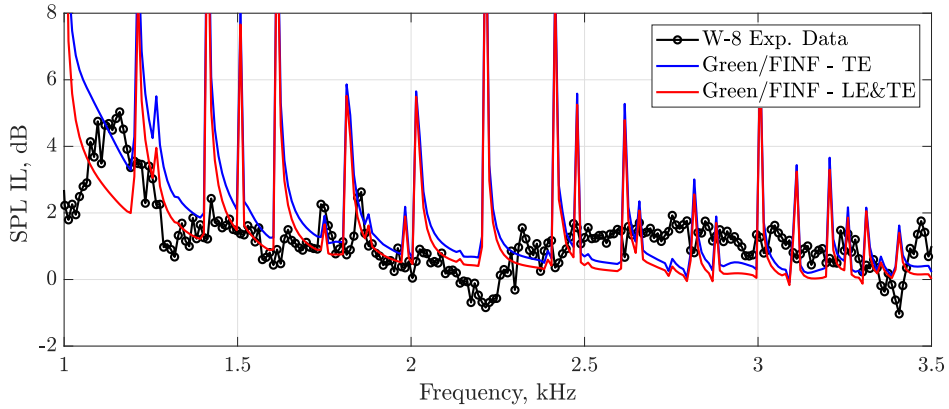

(b) 'Thick' perforate OTR configuration

Fig. 3 Comparison of the measured and predicted SPL IL (hard wall datum) for a distribution of dipoles located at $x_s = 0.75l_L$ (TE) and $x_s = 0.25l_L$ (LE) with M=0.236, $\bar{\Omega} = 0.545$ (50% fan speed), COR=5 and anechoic inlet.

representation of the PWL IL. Both the SPL IL and the PWL IL have been computed for the Green/FINF solution for a 'thin' perforate and are compared to the measured SPL IL in Fig. 4. The overall levels of the two predicted curves ignoring the spikes are similar, differing by around 1 dB, and the PWL IL spectrum shows the same trends as the SPL IL prediction but with less pronounced spikes at the cut-on frequency of each duct mode.

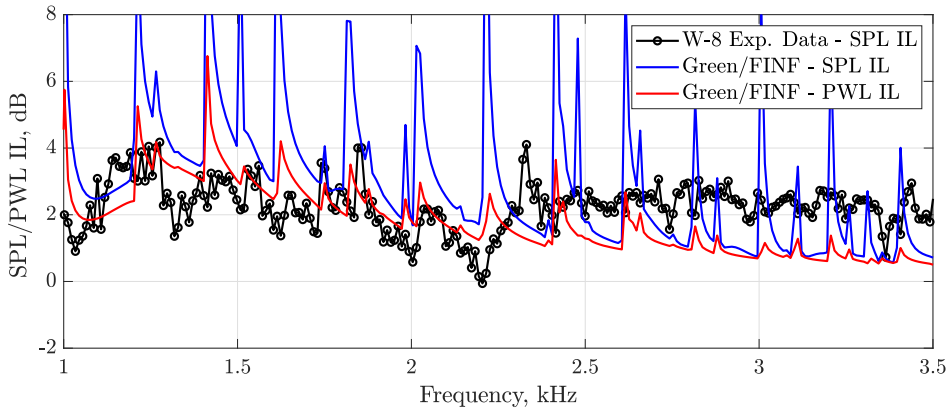

Fig. 4 Comparison of the measured SPL IL and predicted SPL IL and PWL IL (hard wall datum) for the 'thin' perforate and a distribution of LE and TE dipoles with M=0.236, $\bar{\Omega} = 0.545$ (50% fan speed), COR=5 and anechoic inlet.

B. Unflanged inlet termination

The predicted SPL IL and the PWL IL computed for the 'thin' perforates and for the same source as in Fig. 4 have been recomputed for an unflanged inlet termination. The results are shown in Fig. 5. The previous frequency spikes in SPL IL are broadened somewhat but not removed. Indeed a number of additional spikes appear which relate to axial resonances in the inlet hard wall section (region I of Fig. 1). These are caused when the reflected modes from the inlet termination are reflected back at the impedance discontinuity I-II. However, the PWL IL predictions with the unflanged case are less affected by these resonant phenomena than for the anechoic case in Fig. 4 and are in close agreement with the experimental data.

It is still unclear whether an anechoic or unflanged prediction is more appropriate for the W-8 experimental data. This is explored in greater detail in the next section.

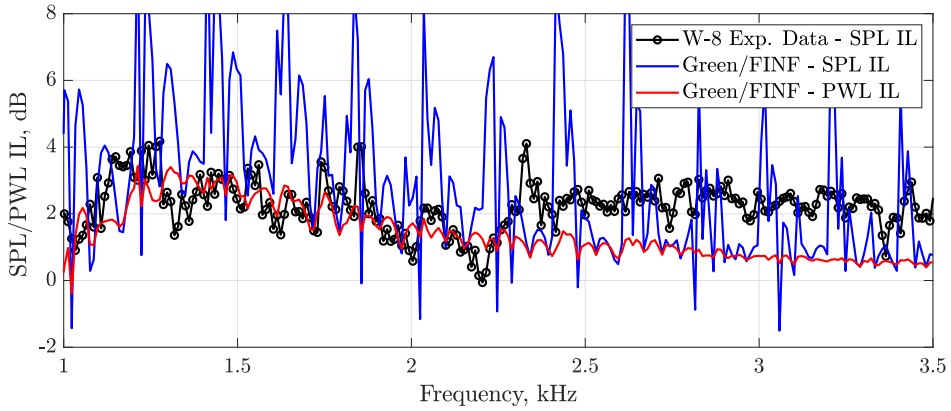

Fig. 5 Comparison of the measured SPL IL and predicted SPL IL and PWL IL for the 'thin' perforate and a distribution of LE and TE dipoles with M=0.236, $\bar{\Omega} = 0.545$ (50% fan speed), COR=5 and unflanged inlet.

V. FE solutions of the W-8 rig and modelling of the termination

An inspection of the W-8 test facility schematic in Fig. 1 of [3] shows that the fan inlet geometry consists of a bellmouth connecting the plenum to the cylindrical section containing the instrumentation and the fan rotor itself. Neither of the previous choices of an anechoic (i.e. no termination at all) or an unflanged (i.e. an abrupt termination at a finite distance from the source) termination in the Green/FIFN model represent well the physical bellmouth intake in the W-8 test facility. An FE model of the W-8 rig was constructed to investigate the effects of including a more realistic duct geometry on the simulated in-duct acoustic field. This is shown in Fig. 6. The 3D model is created by using the commercial software Simcenter 3D Acoustics [14] to reproduce the W-8 geometry with a PML-type boundary condition at the cylindrical exhaust plane and a spherical PML at the bellmouth intake. The guidelines and procedures to generate the mesh and set-up for each configuration follow those described in [31]. In both the numerical model and the analytical solutions the duct exhaust downstream of the source plane is assumed anechoic. This is to approximate the collector system used in the W-8 test facility to exhaust the air from the fan.

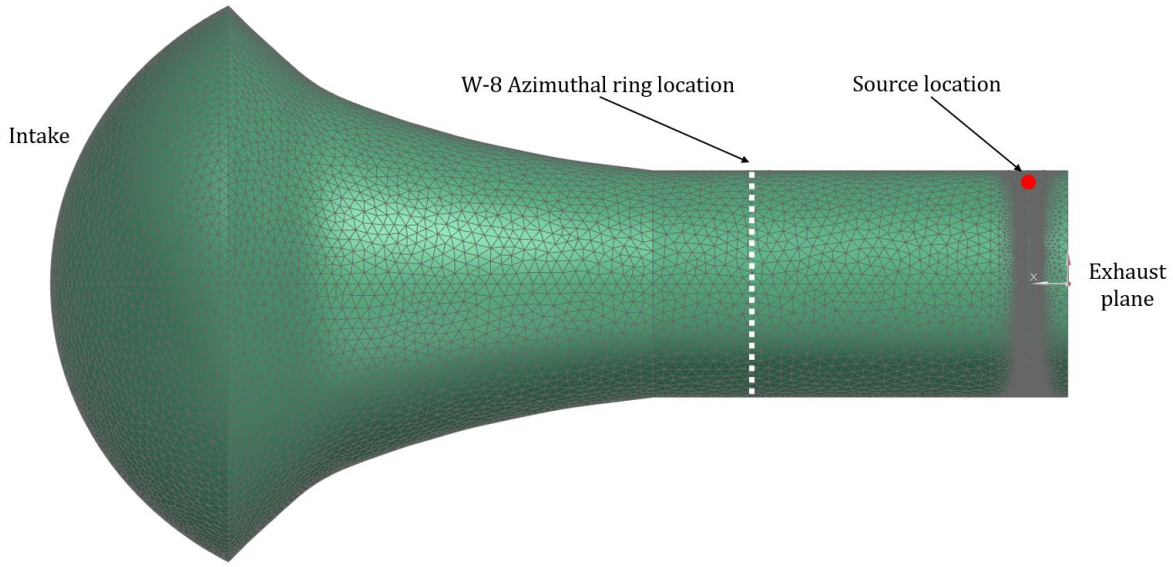

Fig. 6 Diagram of the FE model to study the reflections of the W-8 geometry based on the schematic in [3].

An FE test case has been considered and the results are compared to anechoic and unflanged Green/FINF predictions. Zero flow is assumed. A point volume-velocity monopole is used, which is a simplification of the previous source but which excites the same cut-on/cut-off singularities in the analytical predictions as those which occurs for a 'lift' dipole. This numerical experiment aims to reproduce a sound field generally similar to that of the W-8 experimental arrangement by placing the source at 95% radius, $(x_s, r_s, \theta_s) = (l_L/2, 0.95a, 0)$ in Green/FINF coordinates. Probes are placed on the wall ($r = a$) at the axial location of the W-8 azimuthal microphone array ($x = -2.2a$). The location of the source and the probes is indicated in Fig. 6. Both a hard wall and an OTR lined configuration with impedance $Z = 1$ are considered. The hard wall results are used to assess the effect of cut-on/off singularities on the in-duct field, and the

OTR solution to assess the issue of the axial resonances.

A comparison of the analytical solution and the FE results is shown in Fig. 7 for a frequency range that includes the cut-on frequencies of five higher order modes. Note that all values of m are present in the analytical solutions. All solutions are computed at intervals of 5 Hz. In the hard wall case (Fig. 7a) the FE and Green/FINF anechoic solution show close agreement for most of the spectrum whereas the Green/FINF unflanged solution is not as close.

For the case of an OTR liner (Fig. 7b) the singularities at the cut-on/cut-off frequencies in both the FE and analytic solutions are greatly reduced. When an unflanged termination is considered (labelled Green/FINF-unflanged) however the modes reflected by the inlet termination are reflected back at the impedance discontinuity I-II of Fig. 1 and cause axial resonances and standing waves clearly visible in Fig. 7b. The FE solution and Green/FINF anechoic solution show few signs of such behaviour. The anechoic prediction is generally closer to the FE W-8 results than the unflanged prediction.

The spikes in the SPL IL shown earlier in Fig.5 for the unflanged termination are similar in character to those observed in Fig. 7c. The existence of cut-on/off frequency spikes in both the Green/FINF solutions is largely consistent with their presence in the FE W-8 solution which uses the true inlet geometry. It is unlikely therefore that they are an artifact of the Green/FINF solution procedure. Putting these spikes aside however the correspondence between the FE solutions and the anechoic Green/FINF solutions is close, more so than when the unflanged termination is used. This appears to confirm that the infinite duct is a good approximation of the slow varying bellmouth intake used at the W-8 test rig, matching the higher fidelity FE results somewhat better than the unflanged termination.

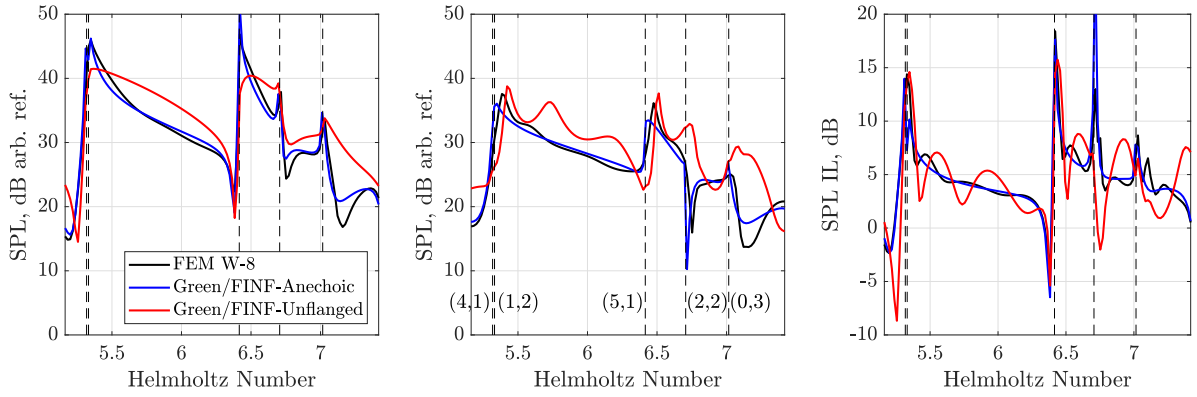

(a) Hard wall **(b) OTR liner** **(c) Insertion Loss**

Fig. 7 Comparison of the FE and predicted SPL and IL spectra with an anechoic/unflanged termination for Case B.

VI. A comment on the SDT RAN test data

Even though there are only weak signs of the cut-on/cut-off spikes in the measured W-8 data, it is interesting to note that in the SDT RAN test data clearer evidence of this phenomenon is present. Unfortunately only hard wall data exist

for this rig. For completeness, the measured hard wall SPL spectra at the wall for the SDT RAN test are compared with Green/FINF predictions for the anechoic and unflanged inlet in Fig.8. The source model used in the predictions is a static axial dipole located at mid-chord position and 95% radius. The azimuthal microphone ring used in the SDT RAN test was installed 0.55 radii upstream of the fan, and the termination is estimated at $x_t/a = -1$. The source SPL level is not known for the analytical model and an arbitrary reference is used in each subfigure for comparison purposes only. Arguably, the unflanged termination is a better representation than the anechoic termination for the flight inlet used in the wind tunnel experiment. Indeed the agreement between the measured and predicted SPL is closer for the unflanged solution (Figs. 8d-8f) than for the anechoic solution (Figs. 8a-8c). Distinct humps can be observed however in the SDT measured data, appearing with a similar periodicity to that of the cut-on/off spikes in the predicted spectra. These are more clearly observed in the predictions with the unflanged inlet. The amplitudes of the predicted singularities are limited when including the reflections at the termination and not far from those of the measured humps. The similar periodicity and amplitudes might suggest evidence of the cut-on singularities in the measured data.

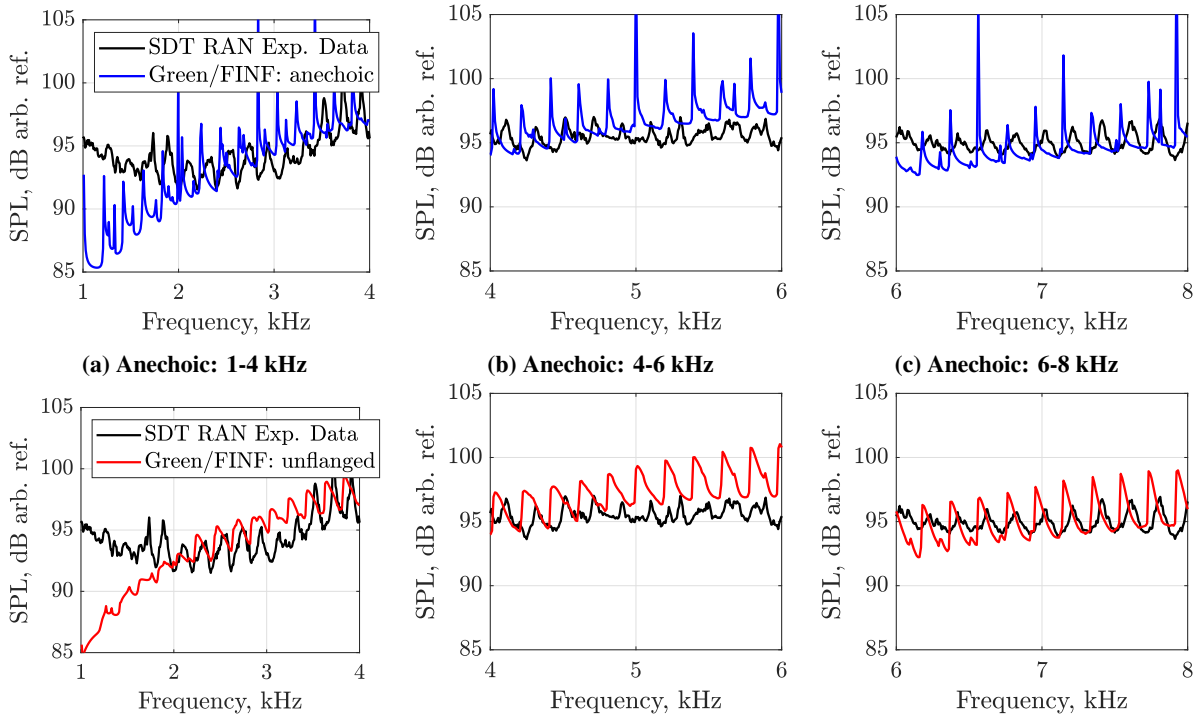

(a) Anechoic: 1-4 kHz **(b) Anechoic: 4-6 kHz** **(c) Anechoic: 6-8 kHz**

(d) Unflanged: 1-4 kHz **(e) Unflanged: 4-6 kHz** **(f) Unflanged: 6-8 kHz**

Fig. 8 Comparison of measured hard wall SPL spectra in the SDT RAN wind tunnel test with predictions for an (a)-(c) anechoic inlet and (d)-(e) unflanged inlet and a static axial dipole at $(x_s, r_s, \theta_s) = (0.5l_L, 0.95a, 0)$ with M=0.236 and COR=5.

VII. Conclusions

An analytic model has been developed to predict the in-duct SPL/PWL Insertion Loss of OTR liners in cylindrical ducts. It includes the coupling of the fan sources to the sound propagation and to the noise suppression. The sources are modelled as distributed rotating dipoles with radially varying strength and stagger angle based on the extension of an existing Green's function for a stationary source in a cylindrical lined duct with uniform mean flow. The model also accounts for the reflections due to the finite, and relatively short, length of the OTR liner and permits an anechoic or unflanged inlet termination. The main conclusions of this work are summarised below:

- The predicted impedance of the lined grooves is found to be in close agreement with the measured impedance in the NASA Langley Normal Incidence Tube.
- Comparisons of the measured SPL IL in the W-8 test rig with the analytical predictions show a reasonable agreement within the 1-2 dB uncertainty of the data.
- For a given OTR liner impedance, a key parameter in the insertion loss prediction model is the axial location of the dominant sources, which controls predominantly the noise attenuation.
- Sharp spikes predicted in SPL and SPL IL in the analytic predictions are much broader and shallower in the measured data, more so in static rig tests with a bellmouth intake (W-8 rig) than in a more realistic flight intake tested in the wind tunnel (SDT RAN).
- A numerical FE study of the W-8 bellmouth geometry has shown that an anechoic intake approximates quite well the slow varying bellmouth intake used in the static rig.
- The measured hard wall SPL spectra from the same fan rotor tested in a more realistic test with a flight intake (SDT RAN) have also been compared to the analytical predictions. Cut-off spikes/humps present in the measured data more closely relate to those observed in the analytical predictions.

This work has improved the physical modelling and general understanding of fan noise sources located close to lined duct walls. It has added the modelling of an inlet termination to the existing Green/FINF model for the prediction of OTR liner noise reductions. The comparison with measured data shows that peak broadband noise estimates can be obtained with the proposed analytical prediction model for realistic parameters given the use of appropriate assumptions for the source distribution.

Appendix A: Comparison of the predicted and measured lined grooved impedance

The acoustically treated circumferential grooves tested in the NASA W-8 rig have been modelled here by an equivalent groove impedance at the main duct - groove interface Z_g. The analytical groove model described in Section III requires as input variables the geometry of the grooves and the facing sheet resistance R_{fs}. This appendix compares the predicted lined grooved impedance for a range of values of resistance to the measured impedance in the NASA Langley Normal Incidence Tube (NIT) [28].

The measured data in Fig. A.1 was obtained by using a tonal source for frequencies between 400 to 3000 Hz and at various SPL levels from 120 dB to 150 dB to assess the non-linearity effects [28]. The liner samples tested in the NIT are rectangular, which restricts the azimuthal propagation in the groove section ② that would normally occur when mounted in the fan casing. Hence, the predicted curves in Fig. A.1 are obtained by using $m = 0$ in Eq. 27.

The results, shown in Fig. A.1, show reasonable agreement between the measurements and predictions for the tested range of resistances, especially for the thick perforate. The effect of additional non-linear losses at high SPL excitation corresponds, as expected, to higher values of facing sheet resistance. Measurements of the dynamic SPL at the fan leading edge for a tip Mach number of M=0.596, corresponding to the 50% fan speed data used in this paper, can be as high as 160 dB [32]. However, data of the SPL at the septum position with the fan in operation, which could be lower, is not available. Based on the impedance and absorption coefficient comparisons a compromise of $R_{fs} = 0.5$ has been taken for the 'thin' perforate and $R_{fs} = 0.7$ for the 'thick' one. A sensitivity study around the chosen resistances showed very limited variability in the PWL IL spectrum and provided confidence in the current choice of parameters.

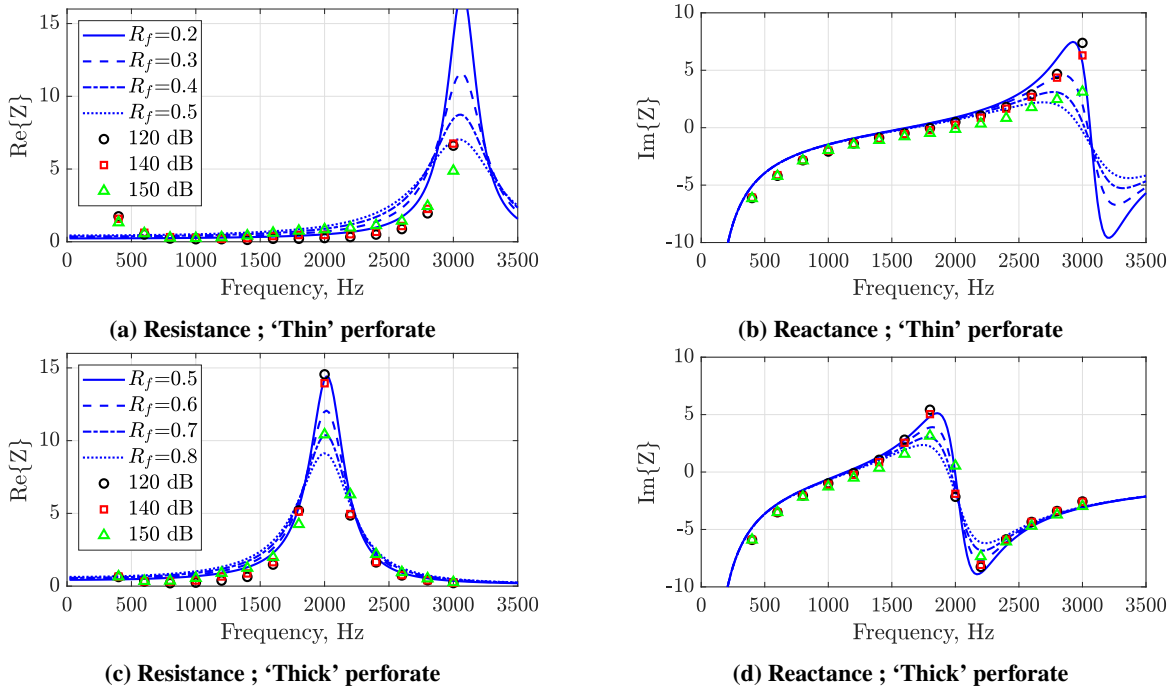

(a) Resistance ; 'Thin' perforate

(b) Reactance ; 'Thin' perforate

(c) Resistance ; 'Thick' perforate

(d) Reactance ; 'Thick' perforate

Fig. A.1 Comparison of the predicted (lines) and measured (symbols) [28] impedance of two lined grooves for a range of facing sheet resistances (R_{fs}).

Appendix B: Measured noise reductions and implications on the OTR model

This appendix reviews the main features of the OTR NASA W-8 test [3] and the measured data, used for the comparisons with the prediction model proposed in this paper. The tests were performed at the W-8 Single-Stage Axial Compressor Facility at the NASA Glenn Research Center using the Source Diagnostic Test (SDT) fan rotor R4, which

consist of 22 blades, 22" in diameter and a design speed of 12657 rpm.

The W-8 test rig is an internal flow facility in which the flow is conditioned by a plenum chamber upstream of the fan and guided through a bellmouth into the cylindrical section containing the instrumentation, the fan and the acoustic treatments. Two types of exhaust can be used, 'atmospheric' and 'altitude'. The former can lead to additional background noise as described below. A schematic of the facility is provided in Fig. B.1. The acoustic measurements were obtained by using a combined circumferential and axial array of wall-mounted microphones. The data used in this paper however is that acquired by using the circumferential array, located in the cylindrical section at 2.2 duct radii upstream of the fan.

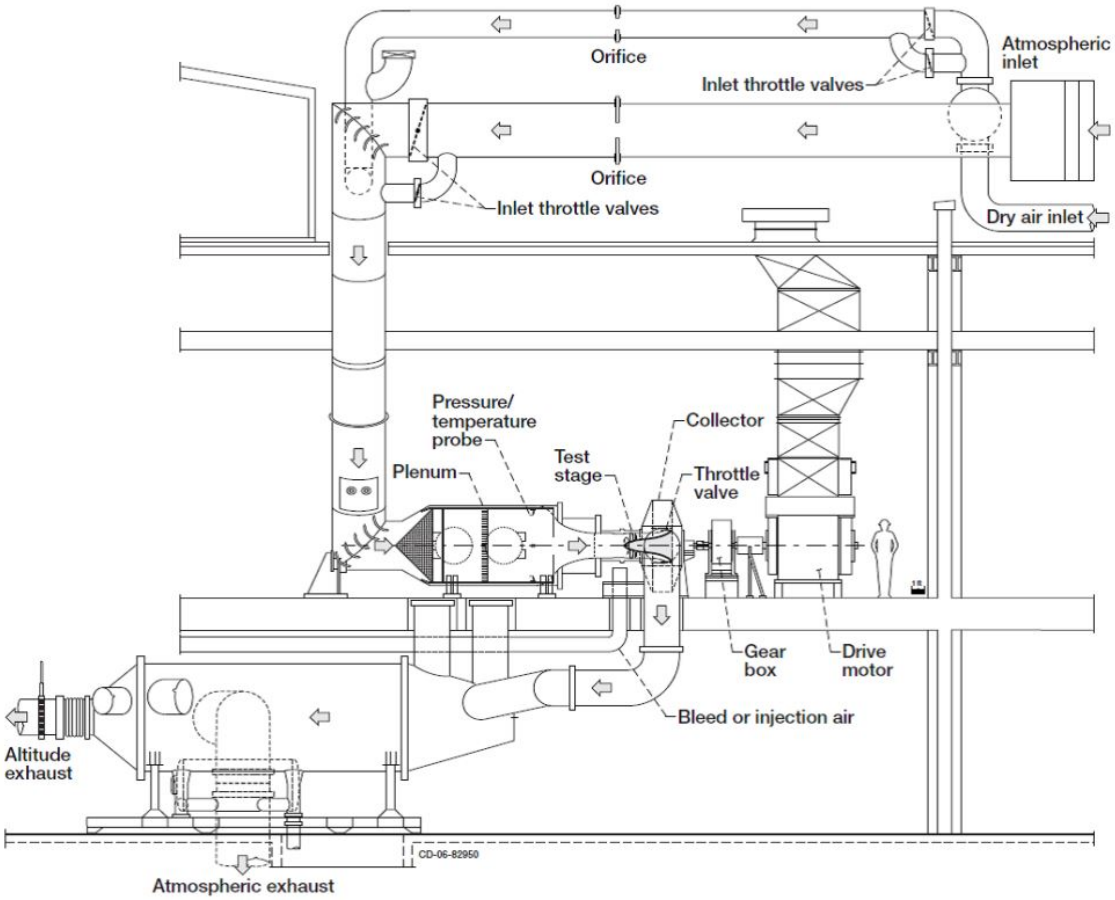

Fig. B.1 Schematic of the W-8 Single Stage Axial Compressor Facility at the NASA Glenn Research Center [3].

The SDT fan rotor R4 was previously tested in a different rig, the Rotor Alone Nacelle (RAN) in the Low Speed Wind Tunnel at NASA GRC, as documented in [33, 34]. Data was collected for the hard wall case. Bozak and Dougherty [3] compared the averaged in-duct Sound Pressure Level (SPL) measured in the W-8 azimuthal ring and that acquired in the RAN configuration, in which an in-duct azimuthal array of microphones upstream of the fan was also installed. Their comparison for the hard wall case is shown in Fig. B.2 to highlight two features of the W-8 data which are key for the

comparison with the analytical predictions. Published photographs of the SDT RAN and W-8 rig are shown in Fig. B.3.

Background noise: A comparison of the spectra measured in the atmospheric and altitude exhaust modes for the hardwall configuration in the W-8 rig showed that, in the atmospheric mode, an additional broadband noise source contributes to the data around 800 Hz and 4 kHz. This noise source associated with the exhaust mode is referred to as a 'background' source in [3] and can be observed in Fig. B.2 by comparing the solid and dashed blue lines. All the measured data with the acoustic treatments contains the effects of this exhaust noise contribution, which is attenuated by the OTR liners. Therefore, the reduction of fan noise cannot be easily extracted at the affected frequencies, and differences between the measured and predicted analytical fan noise reductions could be masked by this exhaust noise source. The comparisons of measured and predicted data have therefore been restricted to frequencies which do not lie in the affected frequency range.

Dominant noise sources: broadened or 'haystacked' tones are observed at Blade Passing Frequency (BPF) and its harmonics in the W-8 in-duct SPL spectra. These do not appear in the SDT RAN results (Fig. B.2). This feature is linked to turbulence present in the flow upstream of the fan in the W-8 rig interacting with the fan rotor blades. Differences in the inlet boundary layer characteristics arise due to the significantly distinct geometry of the bellmouth in the W-8 rig compared to the flight inlet used in the SDT RAN wind tunnel tests. The thicker W-8 boundary layer causes the fan broadband noise in the W-8 to be about 3 dB higher than that in the SDT for frequencies up to 6.5 kHz. Consequently, leading edge (LE) broadband sources are likely to be significant in the OTR predictions when comparing with the W-8 experimental data in addition to trailing edge (TE) noise.

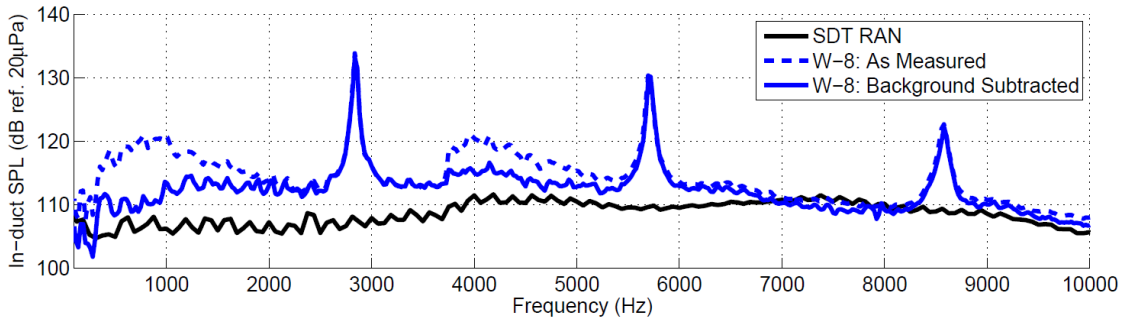

Fig. B.2 Comparison of the SPL spectrum measured with the fan rotor R4 in the SDT RAN and W-8 rigs at 61.7 % speed [3]; hardwall configuration.

Although Sound Power Level (PWL) data was presented in [3] and [33] both for the W-8 and SDT-RAN tests, the comparisons presented here will use only SPL measured data which the authors have full access to. Since the OTR liner was only tested in the W-8 rig, most of the data presented here is taken from that configuration. The measured SPL at the duct wall is shown in Fig. B.4 for the hard wall datum, the hard groove configuration and the two OTR liners ('thin'

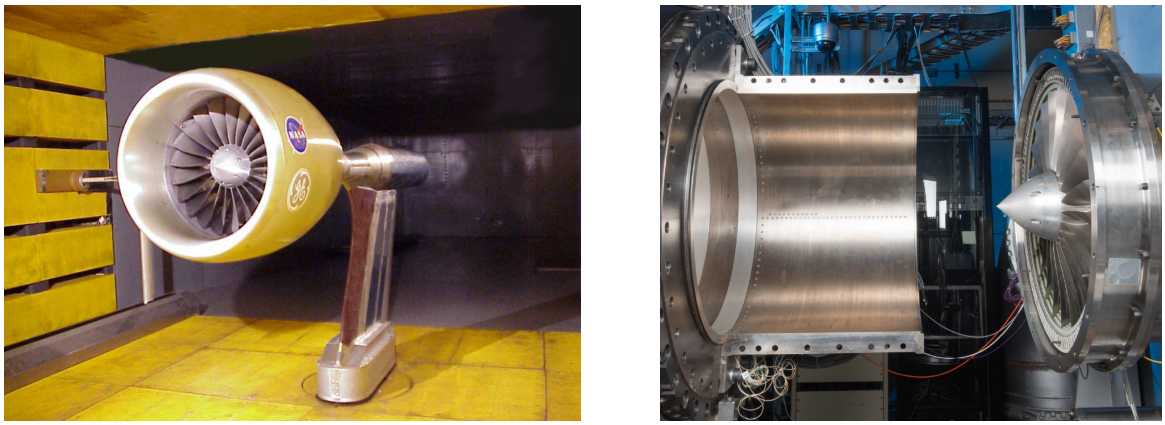

(a) SDT RAN **(b) W-8 rig**

Fig. B.3 Pictures of (a) the NASA SDT RAN in the Low Speed Wind Tunnel at NASA GRC [34] and (b) the NASA W-8 test rig with the fan and case acoustic treatment on the right and the inlet and in-duct array on the left [3].

and 'thick' perforates) described in section III. The location of the two broadband humps of exhaust background noise contaminating the data are roughly indicated at 50 % fan speed with the 'BN' blue arrows. At this fan speed, the hard grooves generate additional broadband noise that becomes dominant at frequencies above 4 kHz, and is attributed to the aerodynamic interaction of the flow in the fan tip region and the grooves. The acoustic treatments in the lined grooves are seen to reduce the additional noise. However, the SPL is still higher than in the hard wall case for frequencies above 5 kHz in the 'thin' perforate and above 4 kHz for the 'thick' one. The area dominated by groove noise is indicated in Fig. B.4 with the red arrow.

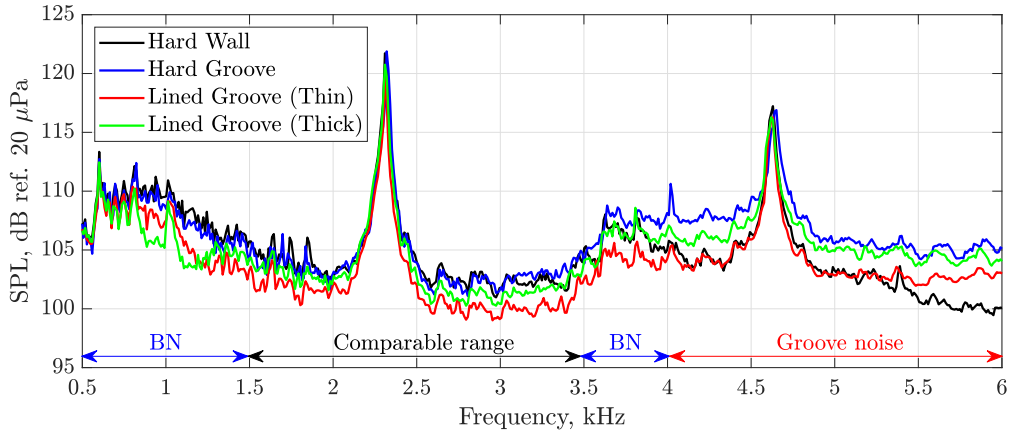

Fig. B.4 W-8 SPL spectra at 50 % fan speed (analysis bandwidth of 5 Hz).

The noise due to grazing flow over the grooves is not modelled by the current analytical impedance groove models, which assume that the uniform mean flow in the duct does not interact with the grooves. It is noted from Fig. B.4 that the effect of the hard grooves in the range of 1.5-3.5 kHz is minimal and relatively free from the background exhaust

noise. Hence, the comparisons between the measured and predicted noise reductions in section IV are restricted to this frequency range to avoid these additional noise sources.

The measured SPL IL based on the hard wall and hard groove datum are shown in Fig. B.5a and Fig. B.5b respectively. The noise reduction spectrum in Fig. B.5a shows more clearly the minimal impact of the hard grooves up to 3.5 kHz, indicated by values of SPL close to zero when a hard groove baseline is considered (blue line), and supports the choice of the frequency range 1.5-3.5 kHz for the comparison with the model. Above this frequency, the additional groove noise dominates and masks the benefits of the OTR liners, a trend that can be observed both for the thin (red line) and thick (green line) liner treatments. However, by assessing the SPL IL with the hard groove datum (Fig. B.5b) it can be observed that the OTR liners are indeed also reducing noise at frequencies above 3.5 kHz by 2-4 dB. The presence of spikes at the Blade Passing Frequency (BPF) and at 2xBPF in the SPL spectra (Fig. B.4) at slightly different frequencies cause the positive and negative spikes in the SPL IL at those frequencies.

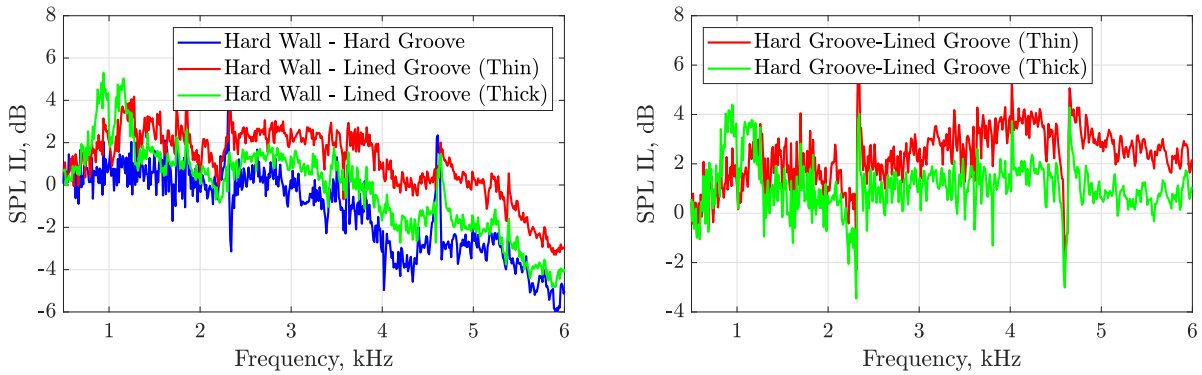

(a) SPL IL - hard wall datum

(b) SPL IL - hard groove datum

Fig. B.5 W-8 SPL IL spectra based on (a) the hard wall datum and (b) the hard groove datum at 50 % fan speed (analysis bandwidth of 5 Hz).

Acknowledgments

This project was funded by the European Union's Horizon 2020 research and innovation programme under a Marie Sklodowska-Curie Innovative Training Network (ITN) grant (Agreement No 722401) within the SmartAnswer consortium. The authors gratefully acknowledge the advice and information provided by Rick Bozak (NASA GRC) and the high-quality fan noise data that NASA has made available for this study. The authors thank Prof. Rienstra for the use of his eigenvalue solver routine, and Dr. Hadrien Beriot for his support in obtaining the numerical solutions using the FE software Simcenter 3D Acoustics. The authors would also like to acknowledge helpful discussions with Emeritus Prof. Morfey.

References

[1] Sutliff, D. L., Jones, M. G., and Hartley, T. C., "High-Speed Turbofan Noise Reduction Using Foam-Metal Liner Over-the-Rotor," *Journal of Aircraft*, Vol. 50, No. 5, 2013, pp. 1491–1503. doi:10.2514/1.C032021, URL http://arc.aiaa.org/doi/10.2514/1.C032021.

[2] Gazella, M. R., Takakura, T., Sutliff, D. L., Bozak, R., and Tester, B. J., "Evaluating the Acoustic Benefits of Over-the-Rotor Acoustic Treatments Installed on the Advanced Noise Control Fan," *23rd AIAA/CEAS Aeroacoustics Conference*, 2017. doi:10.2514/6.2017-3872, URL https://doi.org/10.2514/6.2017-3872.

[3] Bozak, R., and Dougherty, R. P., "Measurement of Noise Reduction from Acoustic Casing Treatments Installed Over a Subscale High Bypass Ratio Turbofan Rotor," *AIAA/CEAS Aeroacoustics Conference*, 2018. doi:10.2514/6.2018-4099, URL https://arc.aiaa.org/doi/10.2514/6.2018-4099.

[4] Bozak, R. F., and Podboy, G. G., "Evaluating the Aerodynamic Impact of Circumferentially Grooved Fan Casing Treatments With Integrated Acoustic Liners on a Turbofan Rotor," *Proceedings of ASME Turbo Expo 2019*, 2019, pp. 1–11.

[5] Hughes, C. E., and Gazzaniga, J. A., "Effect of Two Advanced Noise Reduction Technologies on the Aerodynamic Performance of an Ultra High Bypass Ratio Fan," *15th AIAA/CEAS Aeroacoustics Conference*, 2009, pp. 11–13. doi:doi:10.2514/6.2009-3139, URL http://dx.doi.org/10.2514/6.2009-3139.

[6] Zhang, W., Wang, X., Du, L., and Sun, X., "Mutual effect between swept-and-leaned vanes and acoustic liners on fan interaction-noise reduction," *AIAA Journal*, Vol. 57, No. 6, 2019, pp. 2479–2488. doi:10.2514/1.J057854.

[7] Palleja-Cabre, S., Tester, B. J., Jeremy Astley, R., and Bampanis, G., "Aeroacoustic Assessment of Performance of Overtip Liners in Reducing Airfoil Noise," *AIAA Journal*, Vol. 59, No. 9, 2021, pp. 3622–3637. doi:10.2514/1.j060134.

[8] Bozak, R., Jones, M. G., Howerton, B. M., and Brown, M. C., "Effect of Grazing Flow on Grooved Over-the-Rotor Acoustic Casing Treatments," *25th AIAA/CEAS Aeroacoustics Conference*, 2019. doi:10.2514/6.2019-2564, URL https://doi.org/10.2514/6.2019-2564.

[9] Palleja-Cabre, S., Tester, B. J., Astley, R. J., and Bozak, R., "Modelling of Over-The-Rotor Acoustic Treatments for Improved Noise Suppression in Turbofan Engines," *25th AIAA/CEAS Aeroacoustics Conference*, 2019. doi:10.2514/6.2019-2580, URL https://doi.org/10.2514/6.2019-2580.

[10] Palleja-Cabre, S., Tester, B. J., and Astley, R. J., "Modelling of ducted noise sources in the proximity of acoustic liners," *Journal of Sound and Vibration*, 2021. doi:10.1016/J.JSV.2021.116548, URL https://linkinghub.elsevier.com/retrieve/pii/S0022460X21005708.

[11] Palleja-Cabre, S., Tester, B. J., Astley, R. J., and Beriot, H., "Impedance modelling of acoustically treated circumferential grooves for over-tip-rotor fan noise suppression," *International Journal of Aeroacoustics*, Vol. 19, No. 6-8, 2020, pp. 277–293. doi:10.1177/1475472X20954427, URL https://doi.org/10.1177/1475472X20954427.

[12] Goldstein, M. E., *Aeroacoustics*, McGraw-Hill, New York, [etc.], 1976.

[13] Rienstra, S. W., and Tester, B. J., "An analytic Green's function for a lined circular duct containing uniform mean flow," *Journal of Sound and Vibration*, Vol. 317, No. 3-5, 2008, pp. 994–1016. doi:10.1016/j.jsv.2008.03.048.

[14] "Simcenter 3D 2019.2 Documentation," , 2019. URL https://docs.plm.automation.siemens.com/data_services/resources/scnastran/2019_2/help/tdoc/en_US/pdf/acoustic.pdf.

[15] Ventres, C., Theobald, M., and Mark, W., "Turbofan noise generation. Volume 1: Analysis," Tech. rep., 1982. URL http://ntrs.nasa.gov/search.jsp?R=19830006770.

[16] Lowis, C. R., and Joseph, P. F., "Determining the strength of rotating broadband sources in ducts by inverse methods," *Journal of Sound and Vibration*, Vol. 295, No. 3-5, 2006, pp. 614–632. doi:10.1016/j.jsv.2006.01.031.

[17] Munt, R. M., "The interaction of sound with a subsonic jet issuing from a semi-infinite cylindrical pipe," *Journal of Fluid Mechanics*, Vol. 83, No. 4, 1977, pp. 609–640. doi:10.1017/S0022112077001384.

[18] Munt, R. M., "Acoustic transmission properties of a jet pipe with subsonic jet flow: I. The cold jet reflection coefficient," *Journal of Sound and Vibration*, Vol. 142, No. 3, 1990, pp. 413–436. doi:https://doi.org/10.1016/0022-460X(90)90659-N, URL http://www.sciencedirect.com/science/article/pii/0022460X9090659N.

[19] Rienstra, S. W., "Acoustic radiation from a semi-infinite annular duct in a uniform subsonic mean flow," *Journal of Sound and Vibration*, Vol. 94, No. 2, 1984, pp. 267–288. doi:https://doi.org/10.1016/S0022-460X(84)80036-X, URL http://www.sciencedirect.com/science/article/pii/S0022460X8480036X.

[20] Gabard, G., and Astley, R. J., "Theoretical model for sound radiation from annular jet pipes: Far- and near-field solutions," *Journal of Fluid Mechanics*, Vol. 549, 2006, pp. 315–341. doi:10.1017/S0022112005008037.

[21] Gabard, G., and Astley, R. J., "A computational mode-matching approach for sound propagation in three-dimensional ducts with flow," *Journal of Sound and Vibration*, Vol. 315, No. 4-5, 2008, pp. 1103–1124. doi:10.1016/j.jsv.2008.02.015.

[22] Glegg, S. A. L., "Broadband Generated by Small Fan Noise Turbulence Scale," *NASA Technical Report CR-207752*, 1998.

[23] Glegg, S. A., and Jochault, C., "Broadband self-noise from a ducted fan," *AIAA Journal*, Vol. 36, No. 8, 1998, pp. 1387–1395. doi:10.2514/2.559.

[24] Zhou, Q., and Joseph, P. F., "Frequency-Domain Method for Rotor Self-Noise Prediction," Vol. 44, No. 6, 2006. doi:10.2514/1.16176.

[25] Amiet, R. K., "Noise due to turbulent flow past a trailing edge," *Journal of Sound and Vibration*, Vol. 47, No. 3, 1976, pp. 387–393. doi:10.1016/0022-460X(76)90948-2, URL https://doi.org/10.1016/0022-460X(76)90948-2.

[26] Blake, W. K., *Mechanics of Flow-Induced Sound and Vibration*, 2nd ed., Elsevier Inc, 2017.

[27] Motsigner, R. E., and Kraft, R. K., "Design and Performance of Duct Acoustic Treatment," *Aeroacoustics of Flight Vehicles: Theory and Practice. Vol. 2: Noise Control*, 1991.

[28] Jones, M. G., Nark, D., Howerton, B., and Brown, M. C., "A Review of Acoustic Liner Experimental Characterization at NASA Langley," Tech. Rep. NASA/TP–2020–220583, 2020. doi:10.13140/RG.2.2.15613.10720.

[29] Morfey, C. L., "Sound transmission and generation in ducts with flow," *Journal of Sound and Vibration*, Vol. 14, No. 1, 1971, pp. 37–55. doi:10.1016/0022-460X(71)90506-2.

[30] Joseph, P., Morfey, C. L., and Lowis, C. R., "Multi-mode sound transmission in ducts with flow," *Journal of Sound and Vibration*, Vol. 264, No. 3, 2003, pp. 523–544. doi:10.1016/S0022-460X(02)01205-1.

[31] Bériot, H., Prinn, A., and Gabard, G., "Efficient implementation of high-order finite elements for Helmholtz problems," *International Journal for Numerical Methods in Engineering*, , No. 106, 2016, pp. 213–240. doi:10.1002/nme.5172, URL https://doi.org/10.1002/nme.5172.

[32] Bozak, R., Podboy, G., Dougherty, B., Jones, M., Sutliff, D., and Nark, D., "W-8 Acoustic Casing Treatment Test Overview," *Acoustics Technical Working Group (ATWG) Meeting*, 2017. URL https://ntrs.nasa.gov/citations/20170005682.

[33] Premo, J., Joppa, P., and Company, T. B., "Fan Noise Source Diagnostic Test - Wall Measured Circumferential Array Mode Results," *8th AIAA/CEAS Aeroacoustics Conference & Exhibit*, 2002, pp. 1–13. doi:10.2514/6.2002-2429, URL https://doi.org/10.2514/6.2002-2429.

[34] Hughes, C. E., Jeracki, R. J., Woodward, R. P., and Miller, C. J., "Fan Noise Source Diagnostic Test — Rotor Alone Aerodynamic Performance Results," *8th AIAA/CEAS Aeroacoustics Conference & Exhibit*, 2002. doi:10.2514/6.2002-2426, URL https://doi.org/10.2514/6.2002-2426.